The International Journal of Advanced Manufacturing Technology (2019) 105:565–577
https://doi.org/10.1007/s00170-019-04219-7

ORIGINAL ARTICLE

Analytical modeling of machining-induced residual stresses in milling of complex surface

Ruihu Zhou[1] · Wenyu Yang[1]

Received: 8 March 2019 / Accepted: 31 July 2019 / Published online: 11 August 2019

Abstract
The distribution of residual stresses has a significant effect on fatigue life in milling process. In previous works, the predicted model of residual stresses was focusing on orthogonal cutting, while milling residual stresses is seldom reported. An analytical model for the generation of residual stresses induced by complex surface milling is proposed. Estimates of the mechanical stresses induced by the milling process have been determined through contact mechanics and the geometric transformations within the part. The temperature field of workpiece induced by milling is predicted by analytical model. Estimates of the residual stresses were obtained using an elastic-plastic model and a relaxation procedure. The proposed model is validated with milling experiments. This work can be further applied to improve surface integrity of workpieces by machining parameters optimization.

Keywords Milling temperature · Residual stress · Analytical model · Complex surface milling

1 Introduction

Residual stress is one of the important indicators in surface integrity, which has a great impact on fatigue life of machined workpiece. There were mainly three methods to predict residual stress in machining process: experimental method, finite element method, and analytical method [1]. Li et al. [2] proposed a 3D FEM method to predict milling residual stress using 3D-AdvantEdge and validated by X-ray diffraction method. Yang et al. [3] used a hybrid technique to predict the milling residual stress combining the FEM model. Denkena et al. [4] analyzed residual stress of the 5-axis milling, and explained the effect of mechanical stress and thermal stress. Nespor et al. [5] compared the difference of residual stress between ball-end milling and orthogonal cutting. Wang et al. [6] proposed a FEM model and an empirical model for ball-end milling residual stress prediction. In the previous literatures [2–6], the residual stress in milling mainly carried out by FEM and experimental method, which are difficult to analysis the effect of cutting parameters on residual stress in theory.

As a result, efficient physical-based models for the prediction of residual stress in the machined surface are desperately needed.

The analytical model of residual stress in orthogonal cutting can obtained by following steps: elastic loading, plastic loading, and relaxation procedure, which are introduced in detail by Ulutan et al. [7]. The loading stress is calculated with a sliding/rolling contact model and the relaxation procedure is following boundary conditions, while the loading stress is calculated with a sliding/rolling contact model.

When the analytical model is used to predict the residual stresses in milling, some researchers simplify the 3D milling to 2D orthogonal cutting model supposed helix angle is zero. Su et al. [8] predicted residual stresses in milling process using analytical method. The loading stress calculated is used the maximum pressure for simplification. Huang et al. [9] considered the sequential variable loading in flank milling and obtained the mechanical stress at each tool rotation angle. Peng at al. [10] predicted micro-milling residual stresses using analytical method, considering the milling process characteristics. Zhou et al. [11] developed an analytical model of helical end milling residual stress. The analytical model of cutting force is introduced by Zhou et al. [12], and the temperature field calculated using moving line heat source by Komanduri.R [13]. Fergani et al. [14] predicted residual stress

✉ Wenyu Yang
mewyang@hust.edu.cn

[1] State Key Laboratory of Digital Manufacturing Equipment and Technology, School of Mechanical Science and Engineering, Huazhong University of Science and Technology, Wuhan 430074, China

in multi-pass machining, and the previous toolpath effect is considered. Comprised with orthogonal cutting, the mechanical stress history is cyclic variation with tool rotation angle in milling process, due to the chip thickness varied in milling process. Zeng et al. [15] deduced the residual stress modeling under micro-milling by analytic method considering milling characteristics, such as varied chip thickness and tool rotation. Wan et al. [16] predicted the milling residual stress with a helical helix cutter, also the coordinate transformation is considered in milling process. The above literatures are mainly focusing on three-axis milling process.

For five-axis machining, the cutting parameters are changing instantaneously and more complicated comprised with three-axis milling. To solve this problem, the geometry and kinematics analysis in 5-axis milling with torus-end mill is developed in Section 2. In the previous works [8, 10, 11, 14, 16], the milling temperature field is calculated by the orthogonal cutting temperature model. However, these kinds of simplification lead to errors between predictions and actual results in milling process. In Section 3, an analytical model of milling temperature field is developed based on Lin et al. [17]. In Section 4, residual stresses in milling process are developed based on the orthogonal cutting mechanics and contact mechanics. The experiment results and discussion are introduced in Section 5. Finally, conclusions of this study are summarized in Section 6.

2 Geometry and kinematics analysis in 5-axis milling

2.1 Geometric model of torus-end mill

Geometry of torus-end mill and oblique cutting model is shown in Fig. 1. In Fig. 1 a, the related parameters are defined in the TCS (tool coordinates system) $\{O_T - X_T Y_T Z_T\}$, D is the diameter, r is the radius, $r(z)$ is the cutting radius, O_T is the cutter tip center, n_r is the spindle speed, i_0 is the maximum helix angle, and N_f is the cutter edge number.

The effective cutting radius of point P is the following:

$$r(z) = D - r + \sqrt{r^2 - (r - z)^2} \tag{1}$$

The helix angle of element P is the following:

$$i(z) = cot\left(\frac{(r(z) - (D/2 - r))\tan i_0}{r}\right) \tag{2}$$

The radial lag angle $\psi(z)$ and axial immersion angle $\kappa(z)$ of the point P are following:

$$\psi(z) = \frac{z}{r}\tan i(z), \quad 0 \le z < r \tag{3}$$

$$\kappa(z) = arccos\left(\frac{r - z}{r}\right), \quad 0 \le z < r \tag{4}$$

The radial immersion angle of point P on the jth cutting edge is the following:

$$\phi_j(z) = \varphi + (j-1)^{2\pi}/_{N_f} - \psi(z) \tag{5}$$

where φ is the rotation angle of the reference cutting edge.

As shown in Fig. 1 b, c, and d, the three cutting forces $\{dF_t, dF_r, dF_a\}$ of the infinitesimal element at point P can be derived from the oblique cutting model. In this model, the related parameters and planes are defined in LCS (local coordinate system) $\{P - X_0 Y_0 Z_0\}$. P_s is the cutting plane, P_n is the normal plane, and α_n is the normal rake angle. The inclination angle λ_s is measured in P_s and defined as:

$$\lambda_s = \tan^{-1}(tani \times sin\kappa) \tag{6}$$

In addition, the geometrical parameters associated to oblique cutting and orthogonal cutting model are introduced in detail by Zhou et al. [12]. The fundamental data can obtained in combination with Zhou et al. [12], such as the parameters of shear velocity, shear angle, shear stress, and shear force.

2.2 Five-axis milling process geometry

There are three right-hand Cartesian coordinate systems to describe the five-axis milling process, as shown in Fig. 2 a. The first one is WCS (workpiece coordinate system) $\{O_W - X_W Y_W Z_W\}$. The second coordinate system is FCN (local machining coordinate system) $\{O_T - \mathrm{FCN}\}$. F is the feed direction, N is the surface normal axis of workpiece, and C is determined by F and N. The third coordinate system is the TCS (tool coordinate system) $\{O_T - X_T Y_T Z_T\}$.

The representation of tool path in 5-axis milling is shown in Fig. 2 b. Cutter location file contains a series cutter location points, and each cutter location point is a component with bottom center point $O_{T,t}$, tool axis vector $\mathbf{v}_t$, and feed vector $\mathbf{a}_t$. At time t, $O_{T,t}$ and $\mathbf{v}_t$ can be obtained with linear interpolation method. The feed vector $\mathbf{a}_t$ is the following:

$$\mathbf{a}_t = \frac{{}^W\mathbf{O}_{T,t} - {}^W\mathbf{O}_{T,t-\Delta t}}{\|{}^W\mathbf{O}_{T,t} - {}^W\mathbf{O}_{T,t-\Delta t}\|} \tag{7}$$

In Eq. (7), ${}^W\mathbf{O}_{T,t}$ and ${}^W\mathbf{O}_{T,t-\Delta t}$ are the cutter location vectors at time t and $t - \Delta t$ in WCS, and tool rotation cycle is $\Delta t = \frac{60}{n_r} \cdot \frac{1}{N}$.

The rotation matrix from tool coordinate system to workpiece coordinate system at time t is as follows:

$$\mathbf{R} = \left({}^W\mathbf{x}_{T,t}, {}^W\mathbf{y}_{T,t}, {}^W\mathbf{z}_{T,t}\right) \tag{8}$$

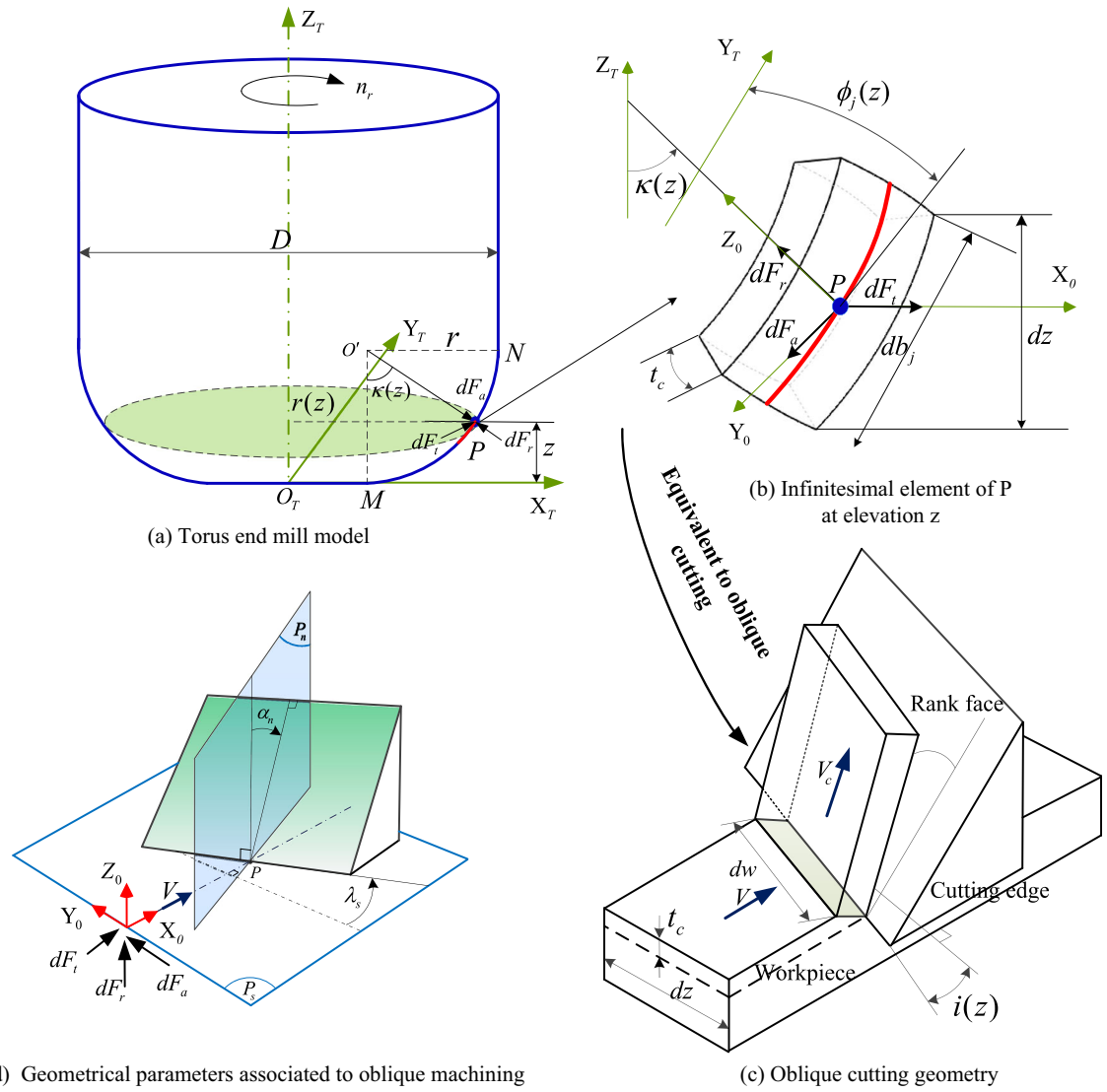

Fig. 1 Geometry of torus-end mill and oblique cutting model. **a** Torus-end mill model. **b** Infinitesimal element of P. **c** Oblique cutting geometry. **d** Geometrical parameters associated to oblique machining at elevation z

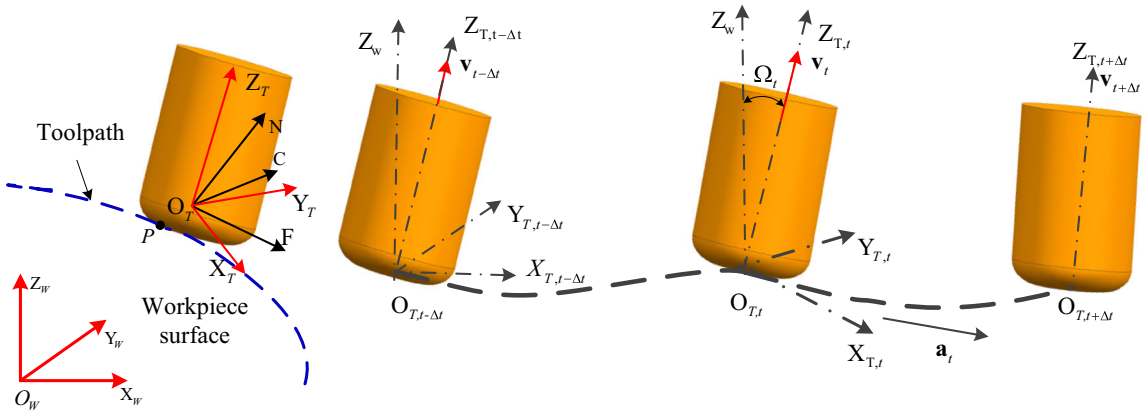

Fig. 2 Coordinate systems and tool path representation in 5-axis machining. **a** Three coordinate systems. **b** Tool path representation in milling

$$\begin{cases} {}^{W}\mathbf{x}_{T,t} = \dfrac{{}^{W}\mathbf{y}_{T,t} \times \mathbf{v}_t}{\|{}^{W}\mathbf{y}_{T,t} \times \mathbf{v}_t\|} \\ {}^{W}\mathbf{y}_{T,t} = \dfrac{\mathbf{v}_t \times \mathbf{a}_t}{\|\mathbf{v}_t \times \mathbf{a}_t\|} \\ {}^{W}\mathbf{z}_{T,t} = \dfrac{\mathbf{v}_t}{\|\mathbf{v}_t\|} \end{cases} \tag{9}$$

In the CL (cutter location) file, each CL data contains 6 parameters (X, Y, Z, I, J, K), the (X, Y, Z) represent the CL point coordinate and (I, J, K) represent tool orientation unit vector. Lead and tilt angles can be calculated as:

$$\begin{aligned} \text{lead} &= \arctan\left(I, \sqrt{J^2 + K^2}\right) \\ \text{tilt} &= \arctan(-J, K) \end{aligned} \tag{10}$$

The relationship between FCN and TCS can be described as follows:

$$\begin{bmatrix} X_{\mathrm{T}} \\ Y_{\mathrm{T}} \\ Z_{\mathrm{T}} \end{bmatrix} = \begin{bmatrix} 1 & 0 & 0 \\ 0 & \cos(\text{tilt}) & -\sin(\text{tilt}) \\ 0 & \sin(\text{tilt}) & \cos(\text{tilt}) \end{bmatrix} \begin{bmatrix} \cos(\text{lead}) & 0 & \sin(\text{lead}) \\ 0 & 1 & 0 \\ -\sin(\text{lead}) & 0 & \cos(\text{lead}) \end{bmatrix} \begin{bmatrix} \mathrm{F} \\ \mathrm{C} \\ \mathrm{N} \end{bmatrix} \tag{11}$$

2.3 Determination of chip thickness

In order to determine whether the cutting edge is involved in cutting, it is necessary to determine the cutting area of the tool and the workpiece. In this paper, z-map method is used to determinate cutter/workpiece engagement which is introduced in detail by Zhu et al. [18].

Uncut chip thickness is the thickness of the material removed instantaneously by the cutting edge in the normal direction. The definition of chip thickness t_{c} is given by Ozturk and Budak [19]:

$$t_{\mathrm{c}} = \mathbf{F}_{\mathrm{t}} \cdot \mathbf{n}_{\mathrm{t}} \tag{12}$$

As shown in Fig. 1 a, the unit outward normal vector $\mathbf{n}(z)$ at point P is:

$$\mathbf{n}(z) = \begin{pmatrix} \left(\sqrt{r^2-(r-z)^2} \cdot \sin\phi_j(z)\right)/r \\ \left(\sqrt{r^2-(r-z)^2} \cdot \phi_j(z)\right)/r \\ (r-z)/r \end{pmatrix} \tag{13}$$

The feed vector in WCS can be determined by the cutter location vector of the cutting edge point P at time $t$and $t - \Delta t$:

$${}^{W}\mathbf{F}_t = {}^{W}\mathbf{P}_{T,t} - {}^{W}\mathbf{P}_{T,t-\Delta t} \tag{14}$$

The feed vector in TCS is the following:

$$\mathbf{F}_t = \left(\mathbf{R}^{-1}\right){}^{W}\mathbf{F}_t \tag{15}$$

3 Prediction of workpiece temperature variation

In this paper, each circular insert is considered sharp, and the cutting tool is supposed to be rigid without deformation. Temperature rise in workpiece caused by the heat sources mainly has three zones: the primary shear zone (chip-workpiece), the second deformation zone (tool-chip), and third deformation zone (tool-workpiece). Only the primary shear zone heat source is considered to predict workpiece temperature variation. In milling process, the tool is discretized the cutting edge into infinitesimal element along tool axis and circular insert number. In addition, cutting time of milling process is discretized into a series of infinitesimal time intervals.

Figure 3 is a heat conduction model considering the heat source of the main shear zone. Each cutting heat source is discretized into rectangular heat source elements. The angle between the shear zone heat source element and its mirror heat source is $2\phi_{\mathrm{n}}$.

The workpiece material is supposed to be isotropic and viscoplastic-rigid, and its behavior is described by the Johnson-Cook constitutive model [12]:

$$\tau_{\mathrm{s}} = \frac{1}{\sqrt{3}}\left[A + B\left(\frac{\gamma}{\sqrt{3}}\right)^{n}\right]\left[1 + C\ln\left(\frac{\dot{\gamma}}{\dot{\gamma}_0}\right)\right]\left[1-\left(\frac{T-T_{\mathrm{r}}}{T_{\mathrm{m}}-T_{\mathrm{r}}}\right)^{m}\right] \tag{16}$$

Furthermore, the shear force dF_{s}, which is proportional to the shear stress τ_{s}, along with the normal force dN_s can be expressed as following [12]:

$$\begin{aligned} dF_{\mathrm{s}} &= \tau_{\mathrm{s}} \frac{dw \cdot t_{\mathrm{c}}}{\cos\lambda_{\mathrm{s}} \sin\phi_{\mathrm{n}}} \\ dN_{\mathrm{s}} &= -\frac{[tan(\phi_n - \alpha_n) + \tan\beta cos\eta_{\mathrm{c}}]\cos\eta_{\mathrm{s}}}{1-\tan\beta\cos\eta_{\mathrm{c}} tan(\phi_{\mathrm{n}} - \alpha_{\mathrm{n}})} dF_{\mathrm{s}} \end{aligned} \tag{17}$$

where t_{c} is the chip thickness that can obtained from Eq.(12), dw is the width of cut, α_{n} is the normal rank angle, β is the friction angle, η_{c} is the chip flow angle, η_{s} is the shear flow angle. Those parameters can be obtained based on Zhou et al. [12] using oblique cutting model and orthogonal cutting model.

For a cutting shear heat source element within each time element, the heat flux density can be calculated by the following:

$$q_{\mathrm{s,j}}(\tau, z) = \frac{R_{\mathrm{w}} V_{\mathrm{s}} dF_{\mathrm{s,j}}(\tau, z)}{(t_{\mathrm{c}}/\sin\phi_{\mathrm{n}})(dz/\cos\lambda_{\mathrm{s}}/\sin\kappa)} \tag{18}$$

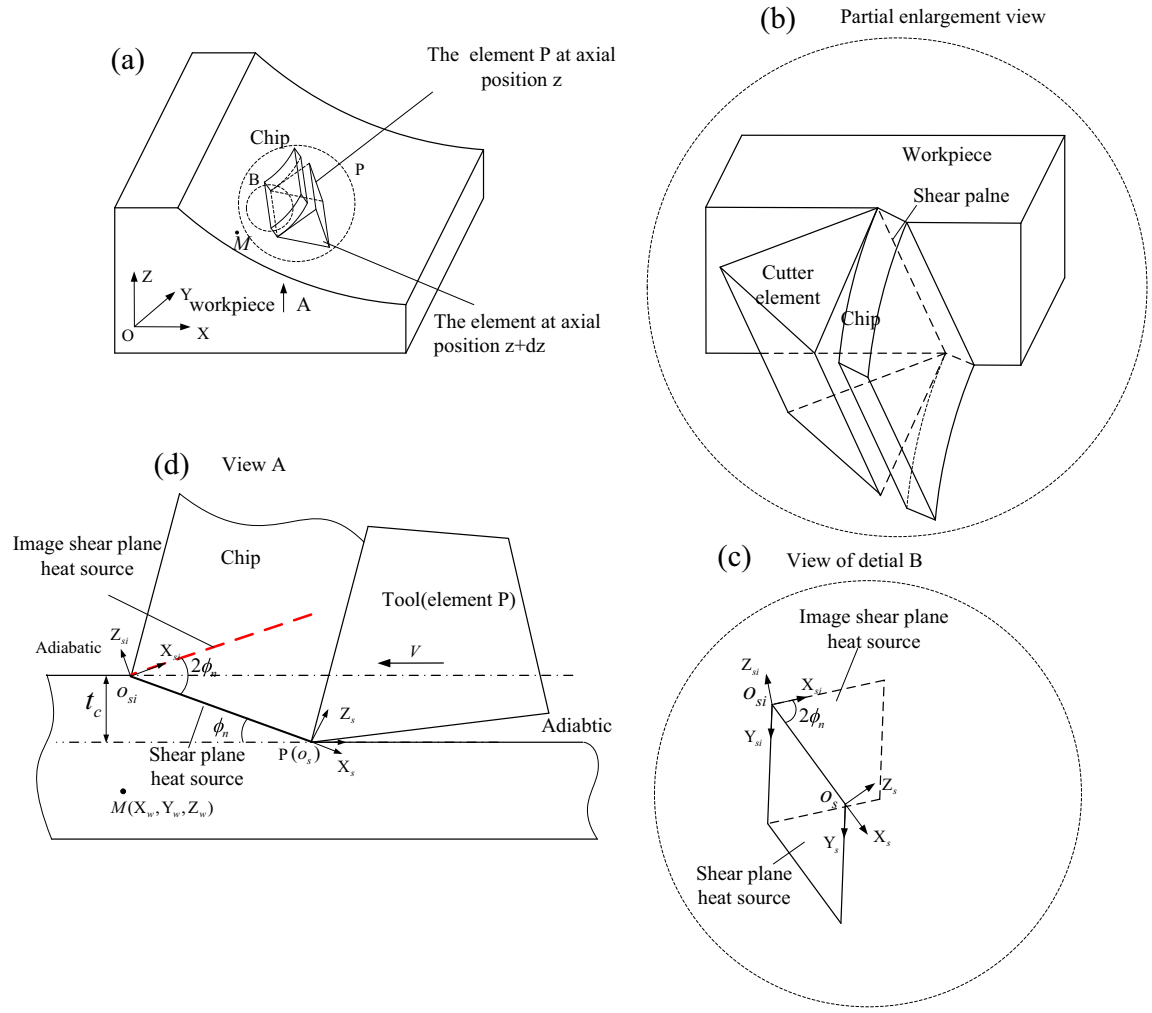

Fig. 3 Heat transfer model and heat partition into workpiece

where $dz/(\sin\kappa \times \cos\lambda_s)$ and $t_c/\sin\phi_n$ are the width and length of elemental shear plane heat source, $dF_{s,j}(\tau, z)$ is the shear force, and V_s is the shear velocity. Those parameters can be obtained based on Zhou et al. [12]. R_w is the heat partition ratio into workpiece.

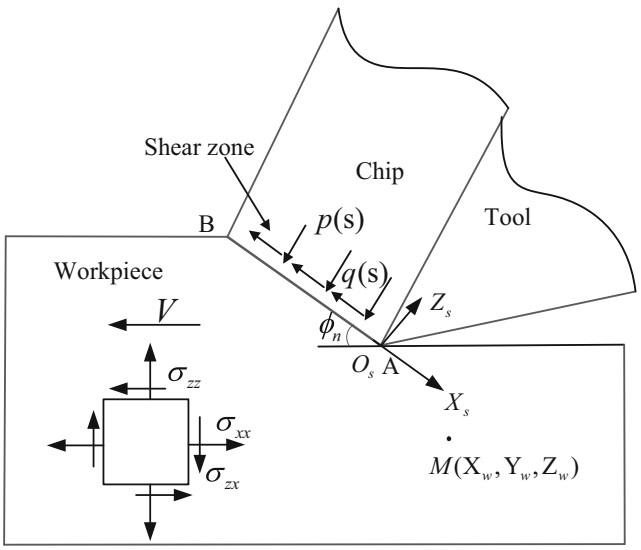

Fig. 4 Stresses field in the shear zone

R_w is the heat partition into workpiece which has been deduced by Shaw M [20]:

$$R_w = 1 - \frac{1}{1 + 1.328\sqrt{\frac{a_w\gamma}{v_c t_c}}} \tag{19}$$

where γ_{sh} is the shear strain, a_w is the thermal diffusivity of workpiece, v_c is the cutting velocity, and γ is the shear strain.

When the cutting edge and cutting time are discretized, the heat source element on the shear zone of each time element can be regarded as a rectangular heat source. In an infinite heat conducting medium, the length and width of the surface heat

Table 1 Johnson-Cook parameters of NAB

A(MPa)	B(MPa)	C	m	n	$\dot{\gamma}_0$ (1/s)	T_m(K)
295	759.5	0.011	1.09	0.405	0.001	1311

Table 2 Physical and mechanical properties of NAB

Property	Elastic modulus (GPa)	Plastic modulus (GPa)	Poisson ratio	Density (kg/m^3)	Specific heat (J/kg/K)	Thermal conductivity (W/m/K)	Coefficient of thermal expansion (1/K)
Parameter	110	80	0.32	7530	419	41.9	1.62×10^{-5}

source are$L$ and W, and its heat flux density value is $q_{s,j}$. After τ, the instantaneous rectangular heat source is heated, and the temperature rise at the point $M(x, y, z)$ caused by the heat source is as follows:

$$\theta=\frac{q_{s,j}}{4c\rho(4\pi\alpha\tau)^{1/2}}\left[\mathrm{erf}\left(\frac{x}{\sqrt{4\alpha\tau}}\right)-\mathrm{erf}\left(\frac{x-W}{\sqrt{4\alpha\tau}}\right)\right]\left[\mathrm{erf}\left(\frac{y}{\sqrt{4\alpha\tau}}\right)-\mathrm{erf}\left(\frac{y-L}{\sqrt{4\alpha\tau}}\right)\right]\exp\left(-\frac{z^2}{4\alpha\tau}\right) \tag{20}$$

where α is the thermal diffusivity,ρ is the density, and c is the specific heat capacity.

As is it known, the temperature can be obtain from Eq. (19) in shear plane as shown in Fig. 3. The point $M(X_w, Y_w, Z_w)$ in WCS can be described in shear zone coordinate system and image shear zone coordinate system by coordinate transformation. The transformation diagram of the coordinate system in milling is following steps:

Step 1: $M(X_w, Y_w, Z_w)$ in WCS, after a period of time t, in TCS, can be described as:

$$(X_T, Y_T, Z_T) = \mathbf{R}^{-1}(X_w-CLt(1), Y_w-CLt(2), Z_w-CLt(3)) \tag{21}$$

where $CLt(1)$,$CLt(2)$,$CLt(3)$ represent the cutter tip location coordinate at time t, respectively.

Step 2: Point M in LCS can be described as:

$$(X_0, Y_0, Z_0) = R_1^{-1}\left(X_T-r(z)\sin\phi_j, Y_T-r(z)\cos\phi_j, Z_T-z\right) \tag{22}$$

where $R_1=\begin{bmatrix}-\cos\phi_j & -\sin\phi_j\sin\kappa & -\sin\phi_j\cos\kappa\\ \sin\phi_j & -\cos\phi_j\sin\kappa & -\cos\phi_j\cos\kappa\\ 0 & \cos\kappa & -\sin\kappa\end{bmatrix}$

Step 3: Point M in shear zone coordinate system $\{P-X_sY_sZ_s\}$ can be described as:

$$\begin{Bmatrix}X_s\\Y_s\\Z_s\end{Bmatrix}=\begin{pmatrix}\cos\phi_n\cos\lambda_s & \cos\phi_n\sin\lambda_s & -\sin\phi_n\\ -\sin\lambda_s & \cos\lambda_s & 0\\ \sin\phi_n\cos\lambda_s & \sin\phi_n\sin\lambda_s & \cos\phi_n\end{pmatrix}\begin{Bmatrix}X_0\\Y_0\\Z_0\end{Bmatrix} \tag{23}$$

In combination with Eqs. (21), (22), and (23), the value of (X_s, Y_s, Z_s) in shear zone coordinate system can obtained.

Step 4: Point M in image shear zone coordinate system $\{O_{si}-X_{si}Y_{si}Z_{si}\}$ can be described as:

$$\begin{Bmatrix}X_{si}\\Y_{si}\\Z_{si}\end{Bmatrix}=\begin{bmatrix}\cos2\phi_n & 0 & \sin2\phi_n\\ 0 & 1 & 0\\ -\sin2\phi_n & 0 & \cos2\phi_n\end{bmatrix}\begin{Bmatrix}X_s+t_c/\sin\phi_n\\Y_s\\Z_s\end{Bmatrix} \tag{24}$$

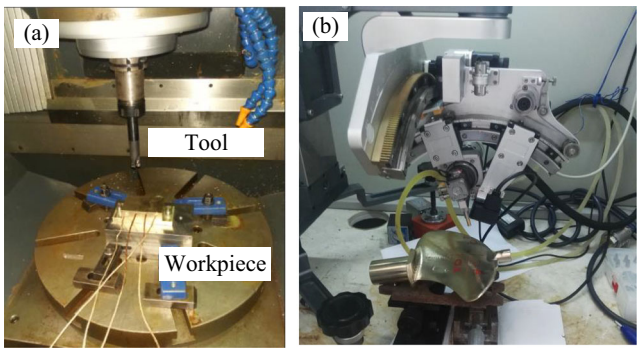

Fig. 5 **a** Milling experiment set-up. **b** X-ray stress analyzer

Table 3 Conditions of X-ray diffraction

Characteristic X-ray	Crk_β
Diffraction plane	<211>
Diffraction angle2θ	152°
Tube voltage	27 KV
Tube current	7 mA
Stress constant$K$	− 180 MPa/°
Scanning angleψ (deg)	0, 15.5, 22.2, 27.6, 32.3, 36.7, 40.9, 45

Table 4 Cutting conditions for milling (slot milling)

No.	Lead (deg)	Tilt (deg)	Spindle speed (rpm)	Feed (mm/tooth)	Cutting depth (mm)
1	0	0	2000	0.05	1
2	0	0	2000	0.1	1
3	0	0	2000	0.15	1
4	0	0	3000	0.1	1
5	5	0	2000	0.1	1
6	0	5	2000	0.1	1

In combination with Eqs. (21), (22), (23), and (24), the value of (X_{si}, Y_{si}, Z_{si}) in shear zone coordinate system can obtained.

The workpiece temperature rise $d\theta$ at time t_s contributed by shear plane heat source is following:

$$d\theta(\tau,z)=\frac{q_{s,j}}{4c_w\rho_w(4\pi\alpha_w(t_s-\tau))^{1/2}}\left[\mathrm{erf}\left(\frac{X_s+t_c\csc\phi_n}{\sqrt{4\alpha_w(t_s-\tau)}}\right)-\mathrm{erf}\left(\frac{X_s}{\sqrt{4\alpha_w(t_s-\tau)}}\right)\right]\left[\mathrm{erf}\left(\frac{Y_s}{\sqrt{4\alpha_w(t_s-\tau)}}\right)-\mathrm{erf}\left(\frac{Y_s-dz\sec\lambda_s}{\sqrt{4\alpha_w(t_s-\tau)}}\right)\right]\exp\left(-\frac{Z_s^2}{4\alpha_w(t_s-\tau)}\right) \tag{25}$$

where α_w,c_w and ρ_w are the thermal diffusivity of heat conductor, the specific heat capacity, and the density of workpiece, respectively.

Similarly, the workpiece temperature rise $d\theta_i$ at time t_s contributed by image shear plane heat source is the following:

$$d\theta_i(\tau,z)=\frac{q_{s,j}}{4c_w\rho_w(4\pi\alpha_w(t_s-\tau))^{1/2}}\left[\mathrm{erf}\left(\frac{X_{si}+t_c\csc\phi_n}{\sqrt{4\alpha_w(t_s-\tau)}}\right)-erf\left(\frac{X_{si}}{\sqrt{4\alpha_w(t_s-\tau)}}\right)\right]\left[\mathrm{erf}\left(\frac{Y_{si}}{\sqrt{4\alpha_w(t_s-\tau)}}\right)-\mathrm{erf}\left(\frac{Y_{si}-dz\sec\lambda_s}{\sqrt{4\alpha_w(t_s-\tau)}}\right)\right]\exp\left(-\frac{Z_{si}^2}{4\alpha_w(t_s-\tau)}\right) \tag{26}$$

The temperature rise of a point $M(X_w, Y_w, Z_w)$ at time t_s can be obtained by integrating Eqs. (25) and (26):

$$T=\sum_{j=1}^{N}\int_0^{a_p}\int_0^{t_s}d\theta(\tau,z)d\tau dz+\sum_{j=1}^{N}\int_0^{a_p}\int_0^{t_s}d\theta_i(\tau,z)d\tau dz \tag{27}$$

where a_p is the cutting depth.

t_s is a definite value, and the temperature rise at the every point of workpiece can be obtained.

4 Residual stresses model of milling process

4.1 Mechanical stress modeling

Using the idea of milling temperature model, discretize the cutting edge into infinitesimal element and cutting time into infinitesimal time interval, the stress field can be obtained in any time. Milling process is oblique cutting process, and plane strain hypothesis can be applied in normal plane shear zone. Notice that in the experiment, both X-ray method and hole drilling method are based on the assumption of plane stress. As a point in complex surface, the stress in normal direction of workpiece surface is approximate to zero, the stress is 2D stress in corresponding tangent plane. The stress field can be described in the local machining coordinate system and the orthogonal cutting model of residual stress can be applied. σ_{xx} is in feed direction and σ_{yy} is in cutting width direction. In combination with Eqs. (11), (22), and (23), The transformation matrix Q of the shear zone coordinate system to the FCN can be obtained.

As shown in Fig. 4, the stress components at point $M(X_w, Y_w, Z_w)$ caused by stress $p(s)$ and $q(s)$ in shear zone can be obtained by rolling contact theory as the following [7]:

$$\begin{cases}\sigma_{xx}=-\frac{2}{\pi}\int_{-AB}^{0}\frac{p(s)(X_s-s)^2Z_s}{\left[(X_s-s)^2+Z_s^2\right]^2}ds-\frac{2}{\pi}\int_{-AB}^{0}\frac{q(s)(X_s-s)^3}{\left[(X_s-s)^2+Z_s^2\right]^2}ds\\ \sigma_{zz}=-\frac{2}{\pi}\int_{-AB}^{0}\frac{p(s)Z_s^3}{\left[(X_s-s)^2+Z_s^2\right]^2}ds-\frac{2}{\pi}\int_{-AB}^{0}\frac{q(s)(X_s-s)Z_s^2}{\left[(X_s-s)^2+Z_s^2\right]^2}ds\\ \sigma_{xz}=-\frac{2}{\pi}\int_{-AB}^{0}\frac{p(s)(X_s-s)Z_s^2}{\left[(X_s-s)^2+Z_s^2\right]^2}ds-\frac{2}{\pi}\int_{-AB}^{0}\frac{q(s)(X_s-s)^2Z_s}{\left[(X_s-s)^2+Z_s^2\right]^2}ds\end{cases} \tag{28}$$

Assuming that the pressure distribution is uniform, the shear pressure and normal pressure are calculated by the following formula [12]:

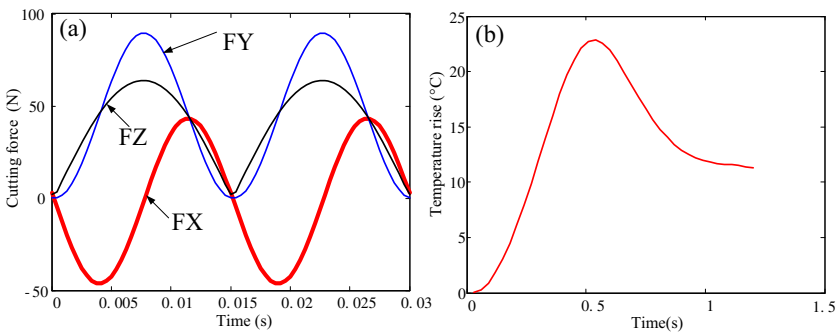

Fig. 6 **a** Cutting force. **b** Temperature rise of point M

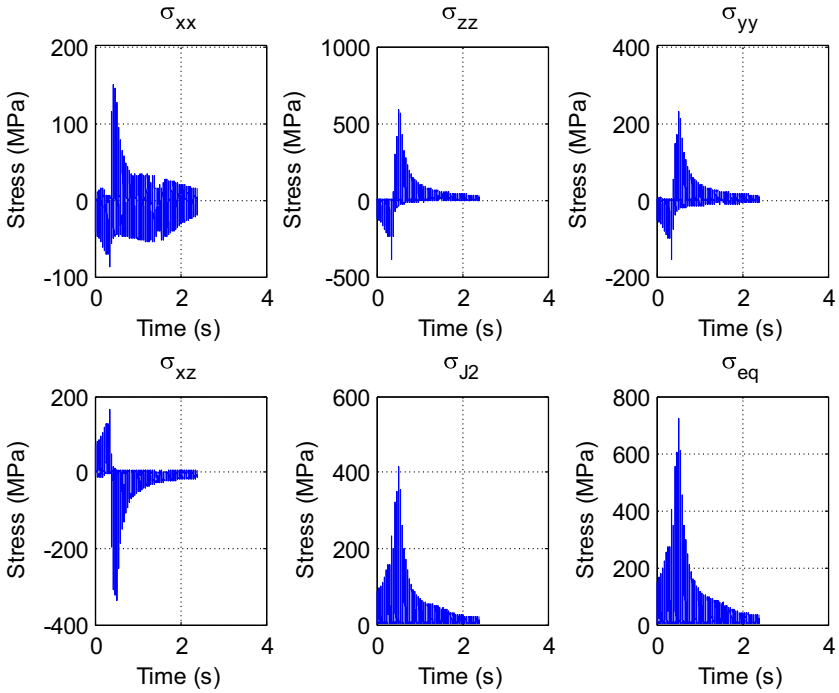

Fig. 7 The history of varied mechanical stress with cutting time

$$\begin{cases} p(s) = \dfrac{[tan(\phi_n - \alpha_n) + \tan\beta cos\eta_c]\cos\eta_s}{1 - \tan\beta\cos\eta_c tan(\phi_n - \alpha_n)}\tau_s \\ q(s) = -\tau_s \end{cases} \tag{29}$$

The integral length is determinated by the instantaneous uncut chip thickness and the shear angle:

$$AB = t_c / \sin\phi_n \tag{30}$$

$[\sigma_s]$ is the stress field in shear zone coordinate system, and $[\sigma_w]$ is the stress field in FCN as follows:

$$[\sigma_w] = Q[\sigma_s]Q^T \tag{31}$$

4.2 Residual stress modeling

Hybrid algorithm is used to calculate the residual stress. A blending function Ψ is the following:

$$\Psi = 1 - \exp\left(-\kappa \frac{3}{2}\frac{h}{G}\right) \tag{32}$$

where κ is an algorithm constant, h is the plastic modulus, and G is the shear modulus.

Yield surface function F is the following:

$$F = \frac{1}{2}\left(S_{ij} - a_{ij}\right)\left(S_{ij} - a_{ij}\right) - k^2 = 0 \tag{33}$$

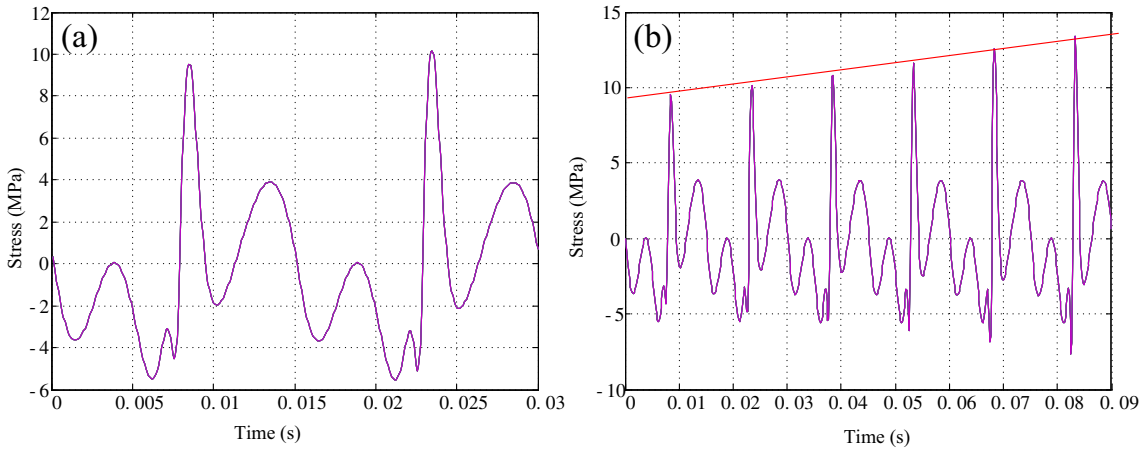

Fig. 8 Mechanical stress σ_{xx} varied with cutting time. **a** In one cycle. **b** In three cycles

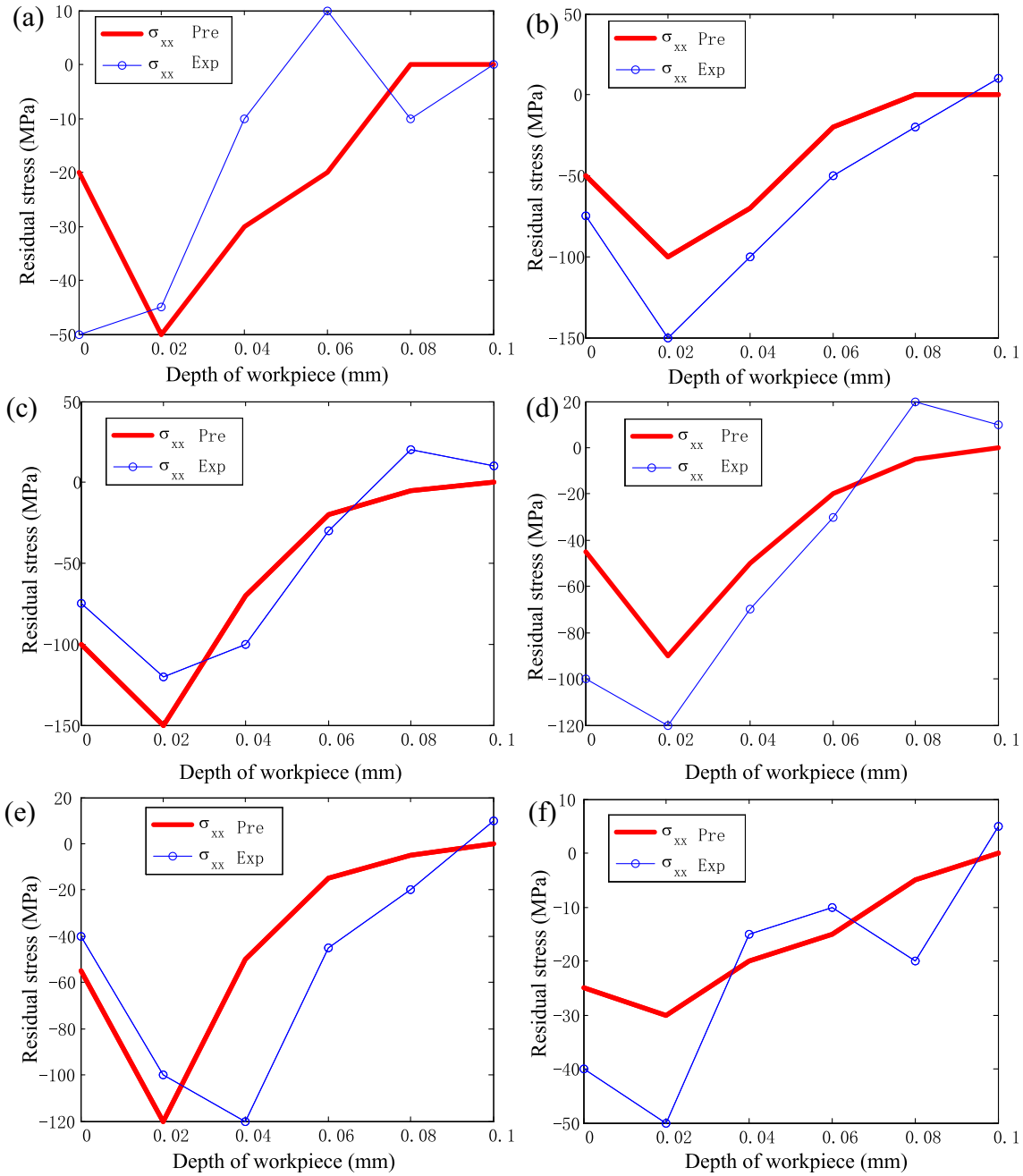

Fig. 9 Residual stresses results in feed direction **a**–**f**: Nos. 1–6

where k is the shear yield strength, S_{ij} are deviatoric stresses, and α_{ij} are back stresses.

The strain rates $d\varepsilon_{xx}$ and $d\varepsilon_{yy}$ are as follows:

$$d\varepsilon_{xx} = \frac{1}{E}\left(d\sigma_{xx}^{pl} - \upsilon\left(d\sigma_{yy}^{pl} + d\sigma_{zz}^{el}\right)\right) + \alpha_T dT + \frac{1}{h}\left(n_{xx}d\sigma_{xx}^{pl} + n_{yy}\sigma_{yy}^{pl} + n_{zz}d\sigma_{zz}^{el} + 2n_{xz}d\sigma_{xz}^{el}\right)n_{xx}$$
$$= \psi\left(\frac{1}{E}\left(d\sigma_{xx}^{el} - \upsilon\left(d\sigma_{yy}^{pl} + d\sigma_{zz}^{el}\right)\right) + \alpha_T dT + \frac{1}{h}\left(n_{xx}d\sigma_{xx}^{el} + n_{yy}\sigma_{yy}^{pl} + n_{zz}d\sigma_{zz}^{el} + 2n_{xz}d\sigma_{xz}^{el}\right)n_{xx}\right) \quad (34)$$

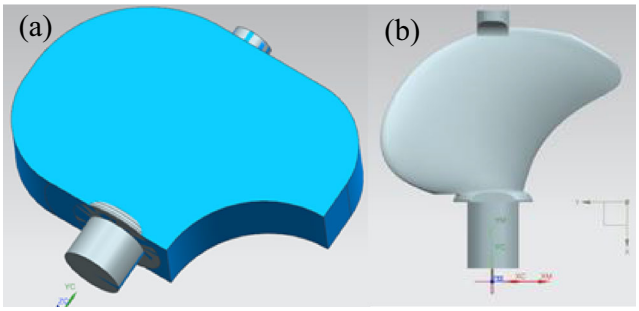

Fig. 10 **a** Block parts. **b** Finished product of CAD model

$$d\varepsilon_{yy} = \frac{1}{E}\left(d\sigma_{yy}^{pl} - \upsilon\left(d\sigma_{xx}^{pl} + d\sigma_{zz}^{el}\right)\right) + \alpha_T dT + \frac{1}{h}\left(n_{xx}d\sigma_{xx}^{pl} + n_{yy}\sigma_{yy}^{pl} + n_{zz}d\sigma_{zz}^{el} + 2n_{xz}d\sigma_{xz}^{el}\right)n_{yy} = 0 \tag{35}$$

where $d\sigma_{ij}^{el}$ is the elastic stress increment, $d\sigma_{ij}^{pl}$ is the plastic stress, α_T is the expansion thermal coefficient, E is the elasticity modulus, υ is the Poisson ratio, dT is the temperature rise increment, and n_{ij} is the component of unit normal in plastic strain rate direction.

A relaxation procedure is introduced by Merwin and Johnson [21]:

$$\begin{aligned} &\sigma_{xx}^{r} = f_1(z),\ \sigma_{yy}^{r} = f_2(z),\ \sigma_{zz}^{r} = \tau_{xz}^{r} = 0 \\ &\varepsilon_{zz}^{r} = f_3(z),\ \varepsilon_{xz}^{r} = f_4(z),\ \varepsilon_{xx}^{r} = \varepsilon_{yy}^{r} = 0 \end{aligned} \tag{36}$$

The increments of nonzero components are followed by M steps:

$$\Delta\varepsilon_{xx}^{r} = \frac{\varepsilon_{xx}^{r}}{M},\quad \Delta\sigma_{zz}^{r} = \frac{\sigma_{zz}^{r}}{M},\quad \Delta\sigma_{xz}^{r} = \frac{\sigma_{xz}^{r}}{M},\quad \Delta T = -\frac{T^{r}}{M} \tag{37}$$

The stress increments $d\sigma_{xx}$ and $d\sigma_{yy}$ are the following (elastic relaxation):

$$\begin{cases} d\sigma_{yy} = \dfrac{-E\upsilon\dfrac{\varepsilon_{xx}^{r}}{M} - (1+\upsilon)\left[\upsilon\dfrac{\sigma_{zz}^{r}}{M} + E\alpha_T dT\right]}{1-\upsilon^2} \\ d\sigma_{xx} = \dfrac{d\sigma_{yy} + \upsilon\left(\dfrac{\sigma_{zz}^{r}}{M}\right) + E\alpha_T dT}{\upsilon} \end{cases} \tag{38}$$

The stress increments $d\sigma_{xx}$ and $d\sigma_{yy}$ are the following (plastic relaxation):

$$\begin{cases} d\sigma_{yy} = \dfrac{\left(-\dfrac{\upsilon}{E} + \dfrac{n_{xx}n_{yy}}{h}\right)Q - \left(\dfrac{1}{E} + \dfrac{n_{xx}^2}{h}\right)W}{\left(-\frac{\upsilon}{E} + \frac{n_{xx}n_{yy}}{h}\right)^2 - \left(\dfrac{1}{E} + \dfrac{n_{xx}^2}{h}\right)\left(\dfrac{1}{E} + \dfrac{n_{yy}^2}{h}\right)} \\ d\sigma_{xx} = \dfrac{W - \left(\dfrac{1}{E} + \dfrac{n_{xx}^2}{h}\right)d\sigma_{yy}}{\left(-\dfrac{\upsilon}{E} + \dfrac{n_{xx}n_{yy}}{h}\right)} \end{cases} \tag{39}$$

where

$$\begin{cases} Q = -\dfrac{\varepsilon_{xx}^{r}}{M} - \dfrac{\upsilon}{E}\dfrac{\sigma_{zz}^{r}}{M} + \dfrac{1}{h}\dfrac{\sigma_{zz}^{r}}{M}n_{zz}n_{xx} + \dfrac{2}{h}\dfrac{\tau_{xz}^{r}}{M}n_{xz}n_{xx} - \alpha_T dT \\ W = \dfrac{\upsilon}{E}\dfrac{\sigma_{zz}^{r}}{M} + \dfrac{1}{h}\dfrac{\sigma_{zz}^{r}}{M}n_{yy}n_{zz} + \dfrac{2}{h}\dfrac{\tau_{xz}^{r}}{M}n_{xz}n_{yy} - \alpha_T dT \end{cases}$$

5 Experimental results and discussion

5.1 Experiment set-up

The workpiece, nickel-aluminum bronze (NAB), is used widely in marine equipment [12]. Table 1 is the Johnson-Cook parameters of NAB. Physical and mechanical properties of NAB are specified in Table 2. In the experiment, the torus cutter type is EMR-C20-4R20-160-2T, with 20-mm diameters, 4-mm bottom radius, and 2 cutter numbers, and cutter install pitch angle is 12°. The circular insert cutter type is Mitsubishi RPMT08T2MOE-JS-VP15TF.

The milling experiments are set-up as shown in Fig. 5 a. After the milling process, the residual stresses was measured with an X-350A X-ray diffraction stress analyzer shown in Fig. 5 b. The electro-polishing technique was used in experiment. In order to avoid the influence of initial residual stress, the initial residual stress is approximately regarded as zero after annealing. The measurement conditions are listed in Table 3.

Table 5 #1 and #2 propeller cutting parameters in finish milling stage (spindle speed(rpm), feed speed(mm/min), cutting depth (mm), cutting width(mm))

Machining region	#1 Suction surface	#1 Pressure surface	#2 Suction surface	#2 Pressure surface
Coolant	yes	no	no	no
Spindle speed	2500	2500	2500	2500
Feed speed	800	800	800	600
Cutting depth	0.5	0.5	0.5	0.5
Cutting Width	0.25	0.25	0.25	0.25

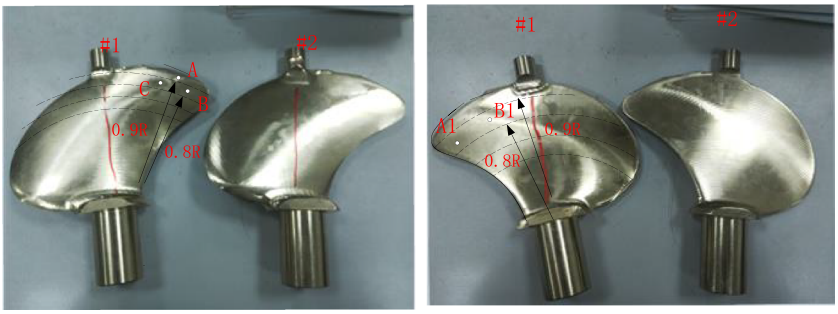

Fig. 11 #1 and #2 model propellers after processing and measured points

5.2 Test 1: simple surface milling

Six groups of cutting parameters are designed in Table 4. The workpiece is block with size 20 × 100 × 100 mm. The workpiece coordinate system is established by taking the initial position of cutter tip as the coordinate origin. The feed direction is the x direction, the normal direction is the z direction perpendicular to the workpiece surface, and the step over direction is the y direction. The point$M(x_w = 10, y = 0, z = 0)$of residual stress with sub-surface is discussed.

Taking No. 2 as an example, the cutting force, temperature, and mechanical stress varied with time are analyzed. Figure 6 is the simulation result of the cutting force and temperature rise. In Fig. 6 a, FX, FY, are FZ are the cutting force in feed direction, cutting width direction, and tool axis direction, respectively. Figure 7 is the process of mechanical stress varied with cutting time, σ_{J2} is the second invariant of stress, and σ_{eq} is the equivalent stress when $\sigma_{J2} < 170$ MPa elastic deformation induced in milling process, and when $\sigma_{J2} > 170$ plastic deformation induced .The value of mechanical stress increases first, then decreases, and then approaches to 0. To further analyze the periodicity of mechanical stress, Fig. 8 describes the variation of stress components σ_{xx} with cutting time. The amplitude varies periodically in one cycle, but the amplitude increases slightly with the increase of cutting time. The reason is that as the distance between the cutter edge and the M point decreases, so the stress value increases.

Figure 9 is the predicted and experiment results of residual stress in feed direction with the depth of workpiece. The results show that the predicted results are consistent with the experimental results. It can be seen that the surface residual stress is compressive stress, and research the maximum amplitude in sub-surface first and decreases with the increase of depth. Comparing the result in Fig. 9 b and c, the residual stress increases when feed rate is increasing. Comparing the result in Fig. 9 b and e, the lead angle has influence on the residual stress. The reason is that the lead angle affects the cutting force and cutting temperature, so the loading stress varied with the lead angle. Also, the tilt angle has the influence on the residual stress shown in Fig. 9 b and f.

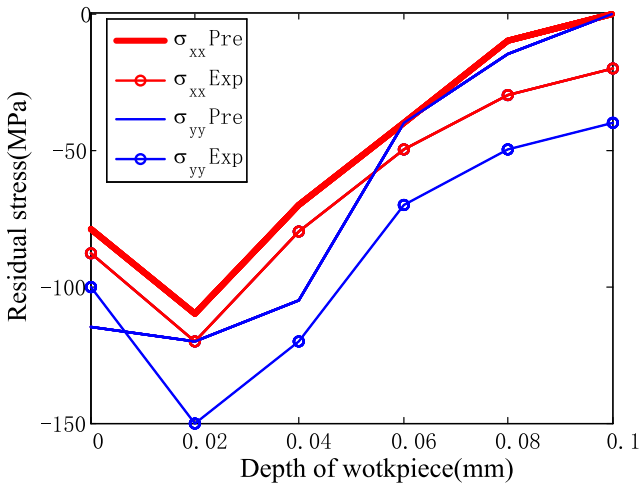

Fig. 12 Results of residual stresses in point M

5.3 Test 2: complex surface milling

The marine propeller is a typical complex surface, which is according to a certain type of controllable pitch propeller and shown in Fig. 10. The workpiece is a block with size 200 × 200 × 50 mm. The main geometric parameters of the propeller are the following: the diameter is 400 mm and the average blade thickness is 5.16 mm.

The pressure surface and suction surface of the blade are machined separately. After roughing, semi-finishing, and finishing the pressure surface, the pressure surface is machined by reversing the blade along the axis 180°. Table 5 is the machining parameters of #1 and #2 propeller in finish milling stage. The milling mode is fixed contour milling in finish milling stage.

Coordinate measuring machine is used in the experiment, in order to ensure that the measuring point is the same as the simulation point. Figure 11 is the propellers after milling process, and selected five points (A, B, C, A1, B1) to measure residual stress. Also, Fig. 11 only shows five points in #1 propeller, but both #1 and #2 selected the same coordinate points.

The complex surface of workpiece is difficult to describe with analytical expression. In conjunction with the NX8.5, a series of coordinate points are placed on the workpiece surface. These points are used to approximately describe the

Table 6 Results of residual stresses in feed direction on the surface

Measured point	#1 propeller		#2 propeller	
	Measured (MPa)	Predicted (MPa)	Measured (MPa)	Predicted (MPa)
A	−88.2 ± 23	− 79	−35.1 ± 20	− 30
B	−139 ± 15	− 103	−78.9 ± 32	− 78
C	−96.9 ± 16	− 30	−114.3 ± 19	− 20
A1	−172.8 ± 41	− 140	−133 ± 25	− 110
B1	−152.8 ± 20	− 120	−119 ± 36	− 140

workpiece surface. Z-map method is used to determine the tool whether involved cutting in machining. In experiment, the X-ray incident direction is parallel to surface normal direction. The coordinate origin is the center of the blade radius. Figure 12 is the results of residual stress of point $M(x_w = 87.6, y_w = 164.0, z_w = 4.26)$ in suction surface of #2 propeller. The results show that the predicted results are consistent with the experimental results.

Table 6 is the residual stress test results of the propeller surface point along the feed direction (x direction) at surface. Comparing the predicted results with the experimental results, there is a certain error between the predicted results and the experimental results, and the surface residual stress is compressive stress. Residual stress values are different at different points, because the material removal rate at each point is different, and the cutting force and cutting temperature are different. Comparing the results of residual stress of points A, B, and C in #1 and #2 propellers, residual compressive stress is more easily formed on the surface of the blade when the coolant is added. When adding the coolant, the cutting temperature of the surface will be reduced and the residual tensile stress will be reduced. Comparing with the residual stress of points A1 and B1 in #1 and #2 propellers, it can be seen that the amplitude of residual compressive stress decreases with the feed rate decreasing. The reason is that the cutting force and cutting temperature become smaller when the feed speed is smaller, and the compressive stress caused by the cutting force is dominant.

6 Discussion

In the complex surface milling, the previous toolpath is not considered in the study. The residual stress distribution in the sub-surface is in 0.1-mm depth. So, after the semi-finishing stage, the residual stress distribution in the sub-surface is in 0.1-mm depth. And at the finishing stage, the cutting depth is 0.5 mm. Material with residual stress in the previous stage is removed, so the effect of residual stress in the semi-finishing stage can ignore.

In the X-ray diffraction stress measurement, $\sin^2\psi$ method is used to determine the stress by scanning angle ψ and diffraction angle 2θ. In the calculation, the ideal slope of $\sin^2\psi$ and 2θ is obtained by the least square method according to the set value ψ and measured value 2θ.Then the fitting residual error between each measured value $2\theta_i$ and the ideal straight line fitting value is the main source of the uncertainty of stress measurement value. Also, the detail is introduced by Zhang et al. [22].

7 Conclusion

An analytical model is proposed for the prediction of residual stress in complex surface milling under different cutting conditions. The following conclusions can be summarized:

Step 1: An analytical model for the prediction of milling temperature field is presented. A new method considering the coordinate transformation in milling process, which can obtain the temperature rise of workpiece in five-axis milling.

Step 2: Mechanical stresses field is described in FCN with coordinate transformation in five-axis machining. The residual stresses model is proposed considering mechanical stress and temperature field of workpiece.

Step 3: The residual stress measurement based on X-ray was analyzed and verified by experiment. The influence of cutting parameters on residual stress is analyzed, such as lead/tilt angle, feed rate, and spindle speed.

Funding information This work is supported by the National Key Basic Research Program of China (no. 2014CB046704) and Key Projects in the National Science Technology Pillar Program of China (no. 2014BAB13B01).

References

1. Wan M, Ye X-Y, Wen D-Y, Zhang W (2019) Modeling of machining-induced residual stresses. J Mater Sci 54:1–35

2. Li B, Jiang X, Yang J, Liang SY (2015) Effects of depth of cut on the redistribution of residual stress and distortion during the milling of thin-walled part. J Mater Process Technol 216:223–233
3. Yang D, Liu Z, Ren X, Zhuang P (2016) Hybrid modeling with finite element and statistical methods for residual stress prediction in peripheral milling of titanium alloy Ti-6Al-4V. Int J Mech Sci 108:29–38
4. Denkena B, Nespor D, Böß V, Köhler J (2014) Residual stresses formation after re-contouring of welded Ti-6Al-4V parts by means of 5-axis ball nose end milling. CIRP J Manuf Sci Technol 7:347–360
5. Nespor D, Denkena B, Grove T, Böß V (2015) Differences and similarities between the induced residual stresses after ball end milling and orthogonal cutting of Ti–6Al–4V. J Mater Process Technol 226:15–24
6. Wang J, Zhang D, Wu B, Luo M (2017) Numerical and empirical modelling of machining-induced residual stresses in ball end milling of Inconel 718. Procedia CIRP 58:7–12
7. Ulutan D, Alaca E, Lazoglu I (2007) Analytical modelling of residual stresses in machining. J Mater Process Technol 183:77–87
8. Su J, Young KA, Ma K, Srivatsa S, Morehouse JB, Liang SY (2013) Modeling of residual stresses in milling. Int J Adv Manuf Technol 65(5–8):717–733
9. Huang X, Zhang X, Ding H (2015) An analytical model of residual stress for flank milling of Ti-6Al-4 V. Procedia CIRP 31:287–292
10. Peng F, Dong Q, Yan R, Zhou L, Zha C (2016) Analytical modeling and experimental validation of residual stress in micro-end-milling. Int J Adv Manuf Technol 87:3411–3424
11. Zhou R, Yang W (2017) Analytical modeling of residual stress in helical end milling of nickel-aluminum bronze. Int J Adv Manuf Technol 89:987–996
12. Zhou R, Yang W, Yang K (2016) Force prediction models for helical end milling of nickel-aluminum bronze. Int J Adv Manuf Technol 86:1487–1498
13. Komanduri R, Hou ZB (2000) Thermal modeling of the metal cutting process: Part I-Temperature rise distribution due to shear plane heat source. Int J Mech Sci 42:1715–1752
14. Fergani O, Jiang X, Shao Y, Welo T, Yang J, Liang S (2016) Prediction of residual stress regeneration in multi-pass milling. Int J Adv Manuf Technol 83(5–8):1153–1160
15. Zeng H, Yan R, Peng F, Zhou L, Deng B (2017) An investigation of residual stresses in micro-end-milling considering sequential cuts effect. Int J Adv Manuf Technol 91:3619–3634
16. Wan M, Ye X, Yang Y, Zhang W (2017) Theoretical prediction of machining-induced residual stresses in three-dimensional oblique milling processes. Int J Mech Sci 133:426–437
17. Lin S, Peng F, Wen J, Liu Y, Yan R (2013) An investigation of workpiece temperature variation in end milling considering flank rubbing effect. Int J Mach Tools Manuf 73:71–86
18. Zhu R, Kapoor SG, DeVor RE (2001) Mechanistic modeling of the ball end milling process for five-axis machining of free-form surfaces. J Manuf Sci Eng 123:369–379
19. Ozturk E, Budak E (2007) Modeling of 5-axis milling processes. Mach Sci Technol 11(3):287–311
20. Shaw M (2005) Metal cutting principle (second edition). Oxford university press, Oxford
21. Merwin JE, Johnson KL (1963) An analysis of plastic deformation in rolling contact. Proc Institut Mech Eng 177:676–690
22. Zhang D, He J (2001) Residual Stress analysis by X-ray diffraction and its functions. Xi'an jiaotong university press, Xi'an